Cargo surface fluidity reduces inter-motor mechanical interference, promotes load-sharing and enhances run-lengths in an ATP-dependent manner

Niranjan Sarpangala[a] **and Ajay Gopinathan**[a]

[a]Department of Physics, University of California, Merced, CA 95343

This manuscript was compiled on June 29, 2021

In cells, multiple molecular motors work together to carry membranous cargoes such as vesicles and organelles along a network of cytoskeletal filaments. The fluidity of the cargo surface has been potentially associated with both positive and negative effects in transport, but the physical mechanisms, at the motor and cargo level that might be responsible, are not clear. To explore these mechanisms, we developed a 3D dynamical simulation of cargo transport along microtubules by teams of canonically non-cooperative kinesin-1 motors. We accounted for membrane fluidity by explicitly simulating the Brownian dynamics of motors on the cargo surface. Our results indicate that cargo surface fluidity reduces inter-motor interference and promotes load-sharing thereby decreasing off-rates and enhancing the adaptive recruitment of motors. Along with a cooperative increase in on-rates resulting from the 3D geometry, these effects altogether result in enhanced cargo run-lengths, most significantly at low ATP concentrations with implications for transport *in vivo* and artificial cargo design.

kinesin motors| mechanical interference | cargo surface fluidity | transport

In eukaryotic cells, the intracellular transport of material between various organelles and the cellular and nuclear membranes is critical for cellular function and is an active process facilitated by the consumption of energy (1, 2). A variety of motor proteins including myosins, kinesins and dyneins convert chemical energy from ATP hydrolysis into directed stepping along cytoskeletal protein filaments such as actin filaments and microtubules (1, 3). These motors move in different directions along the filaments typically carrying lipid bilayer vesicles packed with proteins and signaling molecules or even membrane bound organelles such as Golgi and mitochondria (1, 2). Defects in motor function can impair normal cell functioning and lead to a variety of pathologies including neurodegenerative diseases like Alzheimer's disease and ALS (4–9). Given its importance *in vivo*, there has been a lot of work done over the years in understanding motor function in the transport context ranging from single molecule studies that elucidate the detailed mechanistic workings of motors (10–17) to the functioning of multiple motors and their co-ordination (18–27). Several theoretical and *in vitro* experimental studies (28–32) indicate that the collective behavior of motors is critically influenced by the elastic compliance of their coupling to each other resulting in observable effects in transport speeds and run lengths. For example, it is known that non-cooperative kinesin motors coupled together by a rigid cargo interfere with each other's functioning leading to enhanced detachments and lowered run lengths (28–30). However, *in vivo* cargoes such as membrane-bound vesicles and organelles are typically carried over long distances by teams of kinesin motors (33, 34). It is possible that the fluid membrane based coupling of motors is critical for reducing interference though this is not as extensively studied or well understood. Studies on transport *in vivo* address this issue inherently, but the environmental complexity makes it difficult to disentangle fundamental phenomena of physical origin due to fluid coupling from the effects of other regulatory mechanisms (35). *In vitro* systems, which offer cleaner insights, include microtubule gliding assays on flat bilayers with embedded motors (36–38), motor driven nanotube extraction from vesicles (39) and more recently even membrane covered beads carried by kinesin motors (40). Studies of these systems and related models have generated a variety of interesting results including increases, decreases and no effects on cargo run lengths and velocities due to membrane fluidity (36, 40–42). These results are obtained under different conditions of cargo geometry, motor density, cargo surface fluidity and environmental factors like ATP concentration. In order to reconcile them, we need an understanding of the relative importance and interplay of these factors and their effects on the number of engaged motors and the loads they experience, which in turn influences their collective speed and processivity.

Here, we used Brownian dynamics simulations to model the transport of a spherical cargo with a fluid surface carried

Significance Statement

Teams of molecular motors carry cargoes like vesicles and organelles with fluid surfaces along a network of cytoskeletal filaments within cells. How the fluidity of the cargo surface affects teamwork among motors that tend to interfere with each other is not fully understood. To explore these questions, we developed a 3D dynamical simulation of cargo transport by teams of kinesin-1 motors along microtubule filaments that explicitly accounts for cargo surface fluidity. We show that fluidity reduces inter-motor interference and promotes load-sharing thereby decreasing motor detachment rates and enhancing the recruitment of more motors. Along with a co-operative increase in motor attachment rates due to the 3D cargo geometry, these effects altogether result in transport of cargo over longer distances with implications for transport *in vivo*, and artificial cargo design.

[2]To whom correspondence should be addressed. E-mail: agopinathan ucmerced.edu

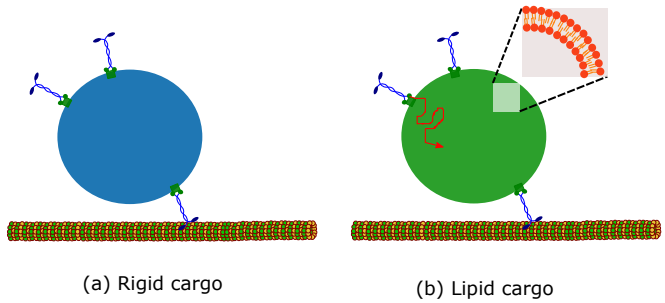

Fig. 1. Two kinds of cargoes considered in the study. (a) Rigid cargo (membrane-free cargo). Molecular motors are permanently attached to random locations on the cargo surface. (b) Fluid/Lipid cargo (membrane-enclosed cargo). Molecular motors can diffuse on the cargo surface. Inset of Fig. 1(b) The lipid bilayer that forms the fluid cargo surface.

by multiple kinesin-1 motors along a microtubule (MT) (see Fig. 1 and details in Materials and Methods). Briefly, we explicitly accounted for the movement of the attachment points of the motors on the cargo surface by allowing free diffusion for unbound motors and diffusion biased by exerted forces for bound motors, with cargo surface fluidity determining the diffusion constant. We also accounted for the force and ATP dependence of the bound motor's off-rate and stepping rate. The spherical cargo's position was then updated by Brownian dynamics depending on the net force exerted by all bound motors. Using this model enabled us to focus on the dynamics of the motors as they diffused on the surface, their binding and unbinding from the filament and the forces experienced by individual motors, as a function of motor diffusion constant, motor density and ATP concentration. We connected these characteristics at the individual motor level to the effect of surface fluidity (inverse viscosity proportional to the diffusion constant) on the collective behavior of motors at the cargo level by analyzing transport properties such as the average number of bound motors, speed and distance traveled (run length). We uncovered two salient features, the reduction of interference and the cooperative increase of on-rates. We showed explicitly that surface fluidity leads to the reduction of negative mechanical interference between kinesins, characterized by lower forces on individual motors and a significant drop in antagonistic forces between motors. This allows teams of fluid-coupled motors to more fully exploit load sharing without inter-motor interference. This decreases single motor off-rates and increases processivity. Interestingly, increasing numbers of bound motors pull the cargo closer to the microtubule, increasing the on-rates of unbound motors, resulting in a cooperative increase in bound motor numbers that depends on 3D cargo geometry. Surface fluidity also makes more motors available for binding, as expected, and as indicated by previous studies (38, 41, 42). However, this effect, by itself, is significant only at lower ATP concentrations (and/or very high motor numbers) when the effective timescale for diffusion and binding is less than the unbinding time. Taken altogether these effects cooperatively result in the run length of lipid cargoes increasing significantly with an increase in fluidity, especially at low ATP concentrations.

Results and Discussions

Surface fluidity reduces negative interference between bound kinesin motors. We first addressed the question of whether the fluidity of the cargo surface has any influence on the functioning of a bound kinesin motor. We expected that the motor attachment point's freedom to move on the lipid cargo surface in response to forces could relieve strain and reduce the forces experienced by the motor. Fig. 2(a) shows a visual comparison of the time traces of the individual motor forces experienced by a team of three bound motors carrying a cargo in the rigid and lipid cases. The noticeably lower magnitudes of the peak forces experienced by the motors in the lipid cases suggest that our expectation is valid. To explore the effect more quantitatively, we computed the distribution of forces experienced by a single motor when it is part of a team of n motors that are simultaneously bound to the microtubule. This distribution, shown for $n = 3$ bound motors in Fig. 2(b), is significantly broader, reflecting larger forces, for a motor on a rigid cargo compared to any of the lipid cargoes. The lipid cargo motor force distributions for different diffusion constants are, in fact, comparable to that for a single bound motor carrying a rigid cargo. A rigid coupling of motors, therefore, results in individual bound motors experiencing higher forces than when they are singly bound to cargo, indicating negative interference. The introduction of surface fluidity reduces this interference by effectively decoupling the motors, consistent with our expectations. This reduction is apparent in the distribution of forces experienced both against (hindering) and in (assistive) the direction of processive motion (Fig. S1). This reduction is also evident in the fraction of "high" forces with a magnitude $\geq 0.01F_s$ (Fig. S2), where F_s is the stall force of kinesin motor (Figs. S3 and S4 show the fractions in hindering and assistive directions). For rigid cargo, this fraction increases as a function of the number of bound motors, n, indicating negative interference between motors. In the presence of surface fluidity, however, no such increase in the high force fraction with n is apparent, indicating a significant reduction of negative interference. In fact, the fraction decreases with n at high surface fluidity ($D = 1\,\mu m^2 s^{-1}$), which is likely due to the decrease in the average force experienced by the motors in the presence of multiple bound motors (Fig. S5). While the decrease in average force occurs for rigid cargo as well, the increase with n due to negative interference dominates.

The variance between the individual forces experienced by simultaneously bound motors is also a measure of negative interference as it quantifies the deviation from perfect load-sharing where the variance is zero. The mean variance over all sampled instances with n bound motors shows a dramatic decrease at higher fluidity ($D = 1\,\mu m^2 s^{-1}$) compared to the rigid cargo case (Fig. 2(c)). In fact, even the presence of a small amount of fluidity accounts for most of the significant drop in variance (Fig. S6) indicating that fairly good load-sharing can be achieved with modest fluidity. We also quantified negative interference more directly by studying whether individual motors were acting antagonistically, i.e., exerting forces in opposite directions. To do this, we computed the correlation between the x-components of bound motor forces $\langle f_x^j f_x^k \rangle$ averaged over different motor pairs (j, k) and time (Fig. 2 (d)). We see that this correlation is highly negative for rigid cargo indicating opposing motor forces while it is negligible in the presence of fluidity indicating motors on

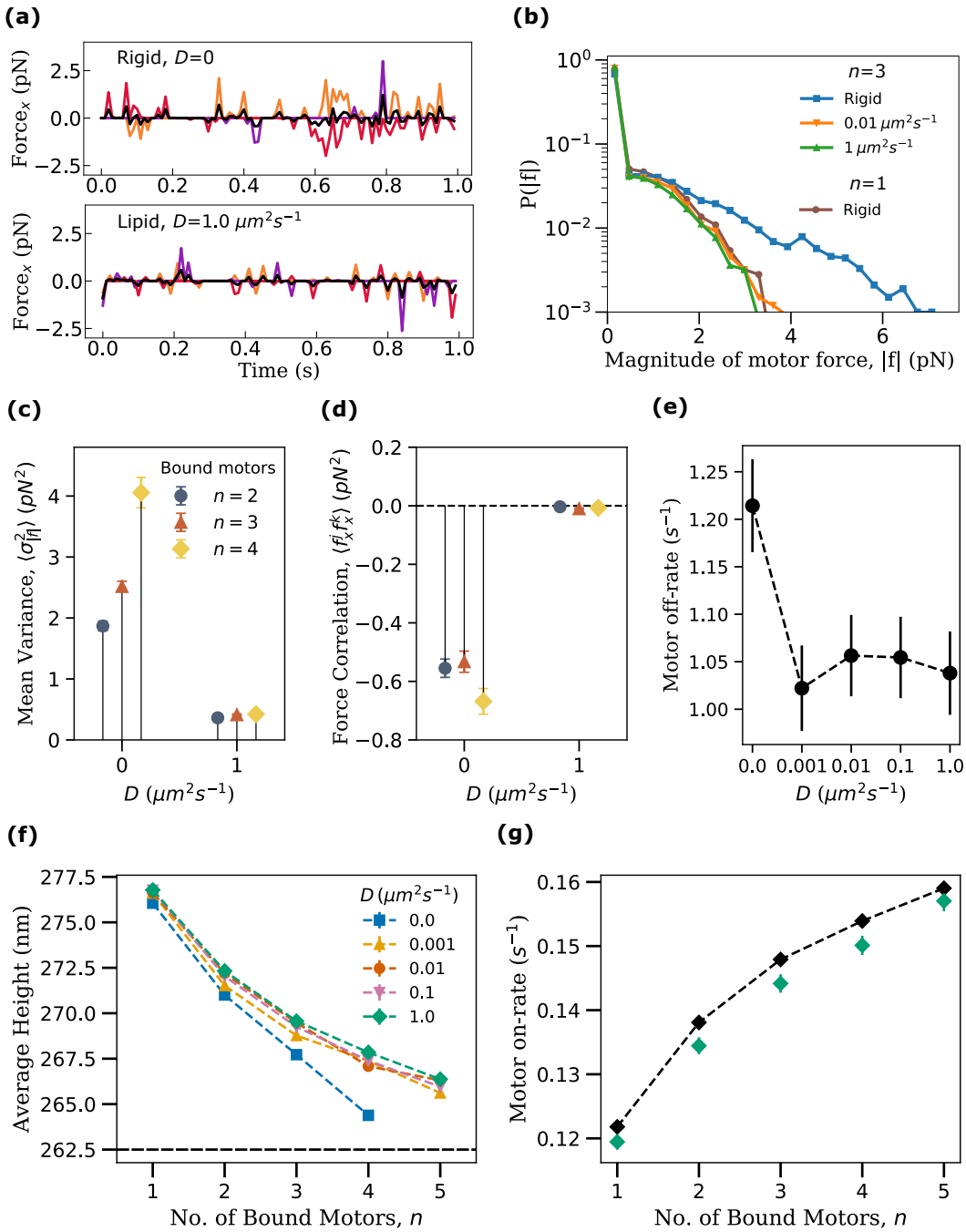

Fig. 2. (a) The x-component of forces experienced by three simultaneously bound motors in rigid (top) and a lipid (bottom) cargoes. Colored curves indicate forces on individual motors, black curve represents the mean of all three. **(b)** Distributions of the magnitude of the force experienced by motors for different cargo surface fluidity at a fixed number of bound motors ($n = 3$). Distribution for singly bound motor carrying a rigid cargo is also shown for comparison. Sample size for each distribution curve was $S = 10000$ time points drawn from 117, 96 and 48 cargo runs for $D = 0, 0.01, 1\ \mu m^2 s^{-1}$ respectively. **(c)** The mean variance of forces among bound motors calculated as $\frac{1}{S}\sum_{i=1}^{S}\sigma^2_{|f|}(i)$ where the summation is over all the sample time points when the number of bound motors is n. $\sigma^2_{|f|}(i)$ is the variance in the magnitude of force experienced by the n bound motors at i^{th} sample. Sample size $S = 10000$ drawn from 200 cargo runs. **(d)** Mean value of the correlation between the x-components of motor forces, $\langle f^j_x f^k_x\rangle$, averaged over motor pairs and time points. Sample size $S = 10000$ drawn from 200 cargo runs. **(e)** Average value of motor off-rate as a function of fluidity of cargo surface ($S = 580$ from 200 cargo runs). **(f)** Average measured distance (h) of the center of mass of cargo from MT as a function of the number of bound motors and fluidity. Horizontal line indicates the height below which the cargo experiences steric interaction from the MT. Data for (a-f) were obtained from the simulation of transport of cargoes with $N = 16$ motors at high ATP concentration of 2 mM. Data sampling rate was 100 s^{-1}. **(g)** Computational measurements of single motor on-rate (green diamonds) and analytical approximation (black dashed line with diamond). ($D = 1\ \mu m^2 s^{-1}$, $S = 10000$) using the cargo height for a given n from the data in (f). Error bars for all plots represent the standard error of the mean.

the same side of the cargo pulling in the same direction. Taken together, our results show that interference dominates over load sharing for rigid cargo while increasing surface fluidity reduces this interference and promotes load-sharing.

Next, we addressed the implications of the reduction in negative interference for the functioning of motors in the context of transport. The off-rate of a kinesin motor increases with the magnitude of the force that it experiences and also depends on its direction (15, 23, 43–45). The observation that surface fluidity reduces negative interference leads us to expect that this will also lead to lower off-rates for individual motors. We measured the mean off-rate of motors as the inverse of the mean time spent by individual motors between a binding and subsequent unbinding event. We found that bound motors on fluid cargoes do indeed have lower off-rates than those on rigid cargoes (Fig 2(e)). Consistent with our findings for the forces and interference, the introduction of a small amount of fluidity accounts for most of the significant drop in off-rates with no significant variation with increasing diffusivity. Thus, increasing surface fluidity reduces inter-motor interference and promotes load-sharing leading to reduced off-rates and potentially longer processive runs for individual motors.

On-rate of a motor increases with the number of bound motors for fluid cargo . The run length of a cargo carried by a team of motors depends on the interplay between the off-rates and on-rates of individual motors (23). The on-rate of a motor, typically considered to be independent of the number of other bound motors, depends on its intrinsic binding rate when it is within reach of the MT. The region of the cargo surface (or access area) from where an anchored kinesin can reach the MT is defined, in our model, by the set of points on the surface at a distance less than or equal to the rest length of the motor ($L_{mot} = 57$ nm). For a cargo bound to the MT with one or more motors, this access area is a function of the cargo geometry and the proximity of the cargo to the MT (38, 46). For rigid cargo, motors can only bind if they happen to be anchored in the access area while for fluid cargo, motors can diffuse in and out of the access area. For a given motor type with a fixed intrinsic binding rate and a given cargo geometry (a sphere here), the access area is then simply a function of the distance of the cargo from the MT. Interestingly, our measurements of the average distance of the center of mass of the cargo from the MT indicated that the cargo comes closer to the microtubule as the number of bound motors increases (Fig. 2(f)). This decrease in distance arises from the increase in the net vertical component of the average force due to an increased number of motors which serves to counteract cargo fluctuations away from the MT. We also note that cargoes with low surface fluidity are closer to the MT than the cargoes with high surface fluidity, especially for high numbers of bound motors. This is because motors on fluid cargoes can relax their tension by sliding on the cargo surface allowing for larger fluctuations (Figs. S7 and S8) and therefore a higher average distance from the MT.

Thus, for both rigid and fluid cargo, as the number of bound motors increases, the cargo approaches the MT leading to an increase in the access area. We expect that this should lead to an increase in the on-rate of an individual unbound motor because its likelihood of being in the access area is increased. We verified this by measuring the on-rate of a motor diffusing on the surface of a cargo held at specific distances from the MT (Fig. 2(g)) that correspond to different numbers of bound motors (from data in Fig. 2(f) for $D = 1\,\mu m^2 s^{-1}$). Here we chose a high diffusion constant for simplicity and measured the mean time required for a randomly placed motor to diffuse and bind to the MT. Indeed, we see that the effective on-rate of the motor, calculated as the inverse of this mean time, increases with decreasing distance corresponding to increasing numbers of bound motors (Fig. 2(g)). To show that the quantitative increase in on-rate was explained by the decreasing distance, we also analytically estimated the change in on-rate. Since the average time spent by a motor in the access area before binding to the microtubule is approximately proportional to the ratio of access area to total area in the high diffusion constant limit, we estimated that the effective on-rate is $\pi_{ad} = \pi_0(S_a/S_T)$, where $\pi_0 = 5\,s^{-1}$ is the intrinsic binding rate, S_a is the access area and $S_T = 4\pi R^2$ is the total surface area of the cargo. By computing the access area numerically for different cargo distances, we were able to estimate π_{ad} corresponding to different numbers of bound motors. The rather good agreement with the measured values from simulations (Fig. 2(g)) indicates that the increase in on-rate is captured by the effects of increased access area. It is to be noted that the rate at which the cargo transitions from being bound by n to $n+1$ motors can be calculated from this on-rate, the off-rate and the number of unbound motors available for binding (details in SI, Section F and Fig. S9).

Our results reveal a positive feedback effect at play. As the number of bound motors increases, the cargo gets closer to the MT and the on-rates of each of the remaining motors increase which further increases the number of bound motors. But a cargo cannot benefit from this positive feedback unless it makes a sufficient number of motors available for binding.

Surface fluidity increases the availability of motors for binding. We expect that the diffusion of motors on the cargo surface should lead to a greater availability of motors in the access region and hence a higher number of bound motors compared to rigid cargo with the same overall number of motors. We also expect that this will be true only if τ_{bind} - the typical time for any one of the unbound motors to bind to the microtubule is less than $\tau_{off} = 1/\epsilon_0$ - the typical time for a given bound motor to detach. The relative values of these two timescales are set by parameters such as the number of motors (N), the radius of cargo (R), and the ATP concentration. For instance, raising the motor density (say by raising N) will result in a higher effective on-rate and a decreased τ_{bind}, while decreasing the ATP concentration, lowers the off-rate and raises τ_{off}.

We first looked at a parameter set (N=16 [ATP]= 2 mM) satisfying the condition $\tau_{bind}<\tau_{off}$ (see SI, Table S1 and Section D, for details of estimates). Fig. 3(a) shows that, while the average number of bound motors, $\bar{n}$, increases with time for both rigid and fluid cargoes, the fluid cargo indeed accumulates more motors. The spatial distribution of motors in Fig. 3(b) further highlights the difference between rigid and fluid cargoes with the probability of finding motors near the microtubule on a fluid cargo being significantly larger at late times than for rigid cargo. It is to be noted that the slight increase at late times for rigid cargoes is simply due to the higher contribution to the average of cargoes, that happen to have motors clustered together, surviving for longer times.

To further test the dependence of motor accumulation on

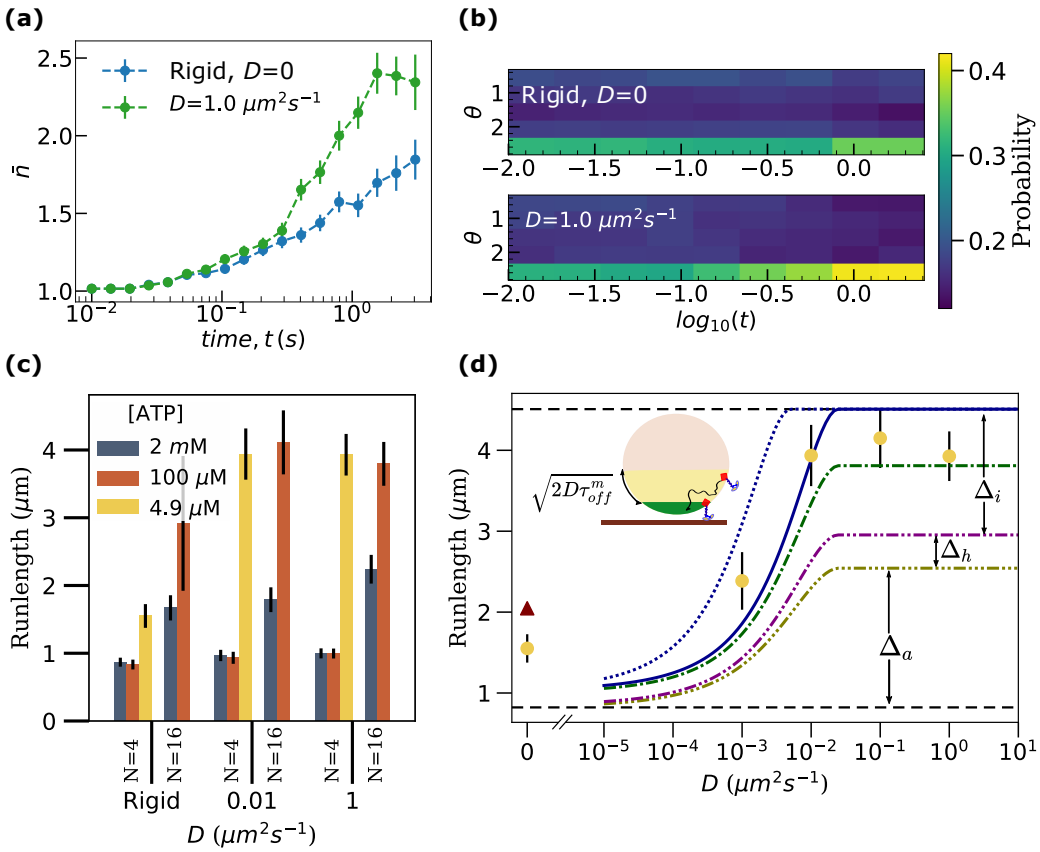

Fig. 3. (a) Ensemble average of the number of bound motors, $\bar{n}$ as a function of time (s). Error bars represent the standard error of the mean. **(b)** Spatial distribution of the kinesin motors on cargo, computed as the probability of locating motors as a function of the polar angle θ and time, t. θ is the polar angle of the motor, measured with respect to z axis perpendicular to the microtubule and passing through the center of the cargo. Data for Fig (a) and (b) was obtained from the transport of cargoes with a total of $N = 16$ motors at [ATP]=2 mM. **(c)** Runlength as a function of diffusivity (D) for two different numbers of motors on the cargo (N) and three different ATP concentrations. 200 cargo runs were considered for each parameter set. Error bars represent the standard error of the mean. **(d)** Comparison between run lengths from our simulations ($N = 4$, [ATP] = 4.9 μM, yellow circles) and analytical estimates (maroon triangle, solid, dashed and dash-dotted lines) as described in the text. $Inset\ cartoon$: A lipid cargo, with access area (S_a, green) and influx area (S_I, yellow) shown. Influx area is defined as the region within $\sqrt{2D\tau^m_{off}}$ from the access area.

the relative values of the two time scales, we considered four other sets of physiologically relevant parameters of N and [ATP] that had different relative magnitudes of τ_{off} and τ_{bind} (shown in Table S1). As predicted, there is no statistically significant difference in the average number of bound motors as a function of diffusivity (see SI, Fig. S11(a)) for cases when $\tau_{off} \approx \tau_{bind}$ ($N = 4$, [ATP]= 2 mM and 100 μM). The number of bound motors, however, increases as a function of diffusion constant (D) for cases where $\tau_{bind} < \tau_{off}$ ($N = 16$ [ATP]= 2 mM and 100 μM, $N = 4$ [ATP]= 4.9 μM) as expected. This supports our expectation that fluid cargoes can indeed accumulate higher number of bound motors than rigid cargoes, but only under conditions that ensure that $\tau_{bind} < \tau_{off}$ i.e. when the number of motors (N) is high or the ATP concentration is low or both.

Fluid cargo have longer run lengths than rigid cargo. So far we have shown that increasing surface fluidity reduces inter-motor interference and promotes load-sharing leading to reduced off-rates. Fluidity also makes more motors available for binding in a cooperative fashion with increased binding leading to higher on-rates. We would expect that having more motors bind that survive longer should lead to increased run lengths for fluid cargo. The run lengths of cargoes measured as a function of diffusion constants (Fig. 3(c)) suggest that this is indeed possible given the right ATP concentration and the number of motors on the cargo (see Fig. S12 for additional diffusion constants). Although the run length is unaffected by fluidity when τ_{bind} is of the order of τ_{off} (low N and medium/high [ATP]), the run length increases with the fluidity of the cargo surface when $\tau_{off} > \tau_{bind}$ (for high N or low [ATP] or both). The effect is much more pronounced when the disparity between the timescales is higher.

We saw earlier that the average number of bound motors shares similar trends (Fig. S11) as a function of cargo surface fluidity. It is to be noted, however, that cargoes can have the same average number of bound motors but different run lengths. For example, although high fluidity (D= 1 $\mu m^2 s^{-1}$) cargoes with $N = 4$ at [ATP]= 4.9 μM and $N = 16$ at [ATP]= 2 mM have the same average number of bound motors, the lower ATP case with fewer total motors shows a substantially larger run length (Figs. S11(a) and S11(b)). This is a consequence of the higher tendency of a cargo to survive a 1 motor state at low ATP due to a lower motor detachment rate (more details in SI, Section E). Overall, our results indicate that surface fluidity increases run lengths when the number of motors (N) is high or the ATP concentration is low or both.

We now consider the relative contribution to the overall run length of the different effects we showed are at play; the reduction in negative interference, the cooperative increase in on-rates and the increased availability of motors.

To estimate the magnitude of these contributions, we first consider an analytical expression for the run length (23)

$$r = \frac{v_o}{N_a \pi_{ad}} \left[\left(1 + \frac{\pi_{ad}}{\epsilon_m} \right)^{N_a} - 1 \right] \qquad [1]$$

where v_o, N_a, π_{ad}, ϵ_m are the motor speed, the available number of motors for transport, the single motor binding rate and the mean motor off-rate respectively. Based on our results, we now generalize the expression by incorporating the dependence of these parameters on the cargo surface diffusivity D and the number of bound motors. The mean off-rate is sensitive to the presence of inter-motor interference and the introduction of fluidity almost completely eliminates interference (Fig. 2(b-e)). This means we can treat the mean off-rate, ϵ_m, as having two values; a higher one for rigid cargo due to interference and a lower one for fluid cargo (Fig. 2(e)). The number of available motors, N_a, is usually taken to be the number of motors in the access area, S_a, for rigid cargo. For $D > 0$, however, additional motors from an influx area S_I (see Fig. 3(d)) can reach the access area before the cargo unbinds from the microtubule and contribute to transport. Here we estimate S_I as defined by a region within a distance $\sqrt{2D\tau^m_{off}}$ of the access area, representing the distance diffused by a motor over the mean motor lifetime $\tau^m_{off} = 1/\epsilon_m$. We, therefore, take N_a to be the average number of motors in the access and influx areas combined, $N_a = 1 + (N-1)(S_I + S_a)/S_T$. Thus the number of available motors starts from a minimum value $N_a = 1 + (N-1)(S_a/S_T)$ at $D = 0$ and increases monotonically as function of D before saturating at $N_a = N$. Finally, motors bind with a rate $\pi_{ad} = \pi_0 = 5\, s^{-1}$ when they are within the access area and do not bind otherwise. This means we can take the mean on-rate of the available motors to be $\pi_{ad} = \pi_0 S_a/(S_I + S_a)$. We note that the access area, S_a, depends on cargo geometry and in particular on the height of the cargo above the microtubule. As more motors bind, the height decreases, S_a increases and the effective on-rate increases (Fig. 2(f-g)). Finally, we note that the cargo velocity did not change by more than 5% over the range of parameters we tested (Fig. S14) and so we took v_o to be constant.

Using these analytic estimates, we can compute approximate bounds for the relative contributions of the different effects to overall run length. As an example, we do this for the case of low motor density and low ATP ($N = 4$ [ATP]= 4.9 μM, Fig. 3(d), other cases in Fig. S16). We start with the limiting lower bound case where there is no additional availability of motors due to diffusion ($N_a = 1 + (N-1)(S_a/S_T)$), no reduction in interference ($\epsilon_m = 0.12\, s^{-1}$, see Fig. S15) and the cargo height is at its maximum (corresponding to having 1 motor bound (Fig. 2(f))). This yields the horizontal dashed line at the bottom in Fig. 3(d). A similar upper bound that assumes all motors are available ($N_a = N$), interference is absent ($\epsilon_m = 0.1\, s^{-1}$, see Fig. S15) and the cargo height corresponds to that at $n = 2$ (which is close to the average number of bound motors for this configuration), yields the horizontal dashed line at the top. While the bounds bracket the run lengths measured from the simulations, we notice that the lower limit is well below the actual values, especially at higher diffusion constants. It is to be noted that the bounds do not really extrapolate well to $D = 0$ because, for rigid cargo, the average run length is not set by the average number of motors in access area. A better approximation is the weighted average of run lengths for different numbers of motors in the access area weighted by the probability of having that many motors in the access area (maroon triangle in Fig. 3(d); details in SI, Section C).

We first consider the contribution due to diffusion increasing the availability of motors alone. Allowing N_a to increase with D but with no reduction in interference ($\epsilon_m = 0.12\, s^{-1}$) and the maximum cargo height, corresponding to $n = 1$, yields the lowest dash-dotted curve in Fig. 3(d). While there is

a substantial increase in run length with increasing D, this increase (of order Δ_a at high D) yields an estimate that is still significantly below the measured values at high D. This indicates that the increased availability of motors alone cannot account for the entire increase in run length. We next incorporate the cooperative increase in the accessible area due to more motors binding and the cargo moving closer to the microtubule by setting the cargo height to that corresponding to $n = 2$ bound motors. This yields an increase in the run length (middle dash-dotted curve in Fig. 3(d)) but the gain, of order Δ_h at high D, is also too small to account for the observed increase. We finally incorporate the effect of reduced interference between the motors due to surface fluidity by taking $\epsilon_m = 0.1\,s^{-1}$. This shifts the run lengths upwards considerably, by Δ_i at high D, and brings the estimates to within the range of the observed values (solid curve in Fig. 3(d); the upper dash-dotted curve is for a cargo height corresponding to one bound motor). Intriguingly, the surface fluidity based reduction in negative interference has an effect that is comparable or even stronger (see Fig. S16 also) than the effect due to the increase in the number of available motors. We note that a reduction in the interference and the resultant reduction in mean off-rate leads to an increase in the mean motor lifetime, τ_m, and hence an increase in the influx area S_I which is set by $\sqrt{2D\tau^m_{off}}$. Thus, reduction in interference contributes to an increased run length not only due to an increased lifetime of each motor but also due to the resultant increase in the number of motors available for transport. While we used the single motor lifetime τ^m_{off} to estimate S_I, this represents a lower bound since new motors may reach the access area over the entire cargo runtime τ^c. Using the saturating value of τ^c (for high D) in place of τ^m_{off} in the expression for S_I therefore gives an upper-bound estimate for the run length (upper dotted curve in Fig. 3(d)). We note that the top three curves for estimates that include the effects of reduced interference and increased availability of motors reflect the measured values of run length fairly well as a function of increasing surface diffusion constant across different conditions of ATP and motor number (see Fig. S16).

Conclusions

Our results show that rigidly coupled motors experience a significantly broader range of forces when multiple motors are bound, reflecting the geometric constraints on the motor-cargo attachment points leading to antagonistic forces and therefore negative mechanical interference between motors. This interference is consistent with literature findings (28–30) and counteracts the expected load-sharing with increasing numbers of motors. We show that the increased fluidity of the lipid membrane which allows the attachment points to move and relax strain, decreases the negative interference between kinesins and permits load-sharing between motors to be more effective. The reduction of negative interference not only contributes almost equally to run length at low ATP (and/or high motor numbers) as increased motor availability but is, in fact, the dominant effect at saturating ATP and low motor numbers (see Fig. S16 a) which is typically the normal physiological (and in vitro experimental) state. Direct measurements of this enhanced load-sharing may be possible using optical trap experiments with an applied load on rigid and fluid cargo. Tuning the load and motor number to a regime where enhanced load-sharing can significantly decrease motor off-rates may be able to resolve the effects in comparisons of rigid versus fluid cargo.

The effects of inter-motor interference in rigid cargo are also expected to be seen in measurements of speed. However, while our measurements of speeds from the simulations do show a decrease with increasing numbers of bound motors (Fig. S14), it is not as dramatic as reported in (40). Consistent with (40), we find this decrease to be negated in the presence of fluidity but the effect is not statistically significant. One possibility is that the force-velocity relation we used (Eq. 11 in Materials and Methods) is not sensitive enough at low loads. Another more intriguing possibility is that the experimentally observed speed-up of lipid cargo (40, 41) may be due to a dispersion of speeds among motors leading to a bias for faster motors in the lead, and slower motors trailing and unbinding more often.

Since the reduction in interference manifests as a decrease in the off-rate of motors, it leads to increasing numbers of bound motors at higher membrane diffusion constants. Interestingly, we found that the on-rate was not constant, but increased with an increasing number of bound motors that effectively pulled the cargo surface closer to the microtubule. Monitoring the binding times of successive motors in an optical trap geometry could potentially allow for the experimental verification this effect. This interesting cooperative effect on the on-rate that we uncovered has a smaller effect, in general, on the run length than the reduced interference or increased availability of motors but is still significant (≈10%), especially at low ATP and/or high motor numbers (see Fig. S16). Thus, while the cooperative increase in on-rates works for both rigid and fluid cargo, the effect is enhanced when more motors are available due to fluidity. Finally, we showed that increased fluidity results in an expected increased recruitment of motors to the microtubule, thereby increasing the number of bound motors, with the effect being significant at very high motor density or low ATP. We found that the confluence of decreased interference, decreased off-rate, increased on-rate and increased motor recruitment can lead to positive feedback resulting in dramatic effects on the run length, under the right conditions. We show, for example, that run length is insensitive to cargo surface fluidity for moderate numbers of motors at saturating ATP but can increase by *several fold* for fluid membranes at low ATP conditions. Taken together, our work reconciles varying experimental results including the observed insensitivity of run length to cargo fluidity at moderate motor densities and high ATP concentrations (40, 41). Our prediction of a significant enhancement of run length at low ATP is potentially physiologically important as an adaptive mechanism, *in vivo*, under stress or starvation conditions (47).

We developed a generalized version of the analytical expression for run length that accounts for cargo surface fluidity and expect it to be useful to explore a wide range of parameter spaces for different motor types and cargo geometries going beyond our simulations, which were done with a fixed cargo radius of 250 nm. Cargo geometry enters into the effective on-rate for motors which scales as $\pi_{ad} = \pi_0 S_a/(S_I + S_a)$. The increase in access area, S_a, as the cargo is pulled closer to the MT is determined by the curvature of the cargo surface and sets the magnitude of the cooperative increase in motor numbers. Even considering a fixed cargo height and high D, the on-rate still depends on the ratio of access area to the

total surface area which decreases with increasing radius of curvature of the cargo. Thus, from our generalized version of Eq. 1, we expect an increased on-rate and higher run lengths for smaller cargo with a fixed number of motors (see Fig. S17), which is consistent with other numerical studies (42). The smallest cargos, with sizes comparable to synaptic vesicles of about 100 nm (48), in fact, show an enormous increase in the run length over a range of fluidity that is consistent with the ranges for *in vivo* membranes in different contexts (49, 50). For synaptic vesicles with fluid membranes therefore, transport over very large axonal distances, is a natural outcome of our model. If the surface density of motors is fixed, on the other hand, the quadratic increase in the number of available motors compensates for the reduction in on-rate resulting in larger run lengths for larger cargo (Fig. S18). In general, the changes in run length over physiological ranges of fluidity imply that surface fluidity could be used as a control parameter to regulate transport.

Our results on the transport properties of fluid cargo over a wide range of surface fluidity, ATP concentration, motor number and cargo size offer quantitative guidelines for the design of artificial cargo driven by kinesin teams. While all our results are specifically using parameters for kinesin motors, they can be readily generalized to other systems with different geometries of cargos with different motors coupled by a fluid surface. Thus our results could be of general value in designing artificial cargo utilizing teams of engineered versions of non-cooperative motors with fluid coupling to enhance load-sharing and processivity. More generally, coupling intrinsically non-cooperative mechanical force-generating elements via a fluid surface could be a generic mechanism to promote load-sharing that is exploited within the cell.

Materials and Methods

Model. We developed a Brownian dynamics model to address the question of how cargo surface fluidity influences transport by teams of kinesin motors. Early models of multi-motor cargo transport used a mean-field approach where all motors were considered to share the load equally (51). Later stochastic models that assume unequal load sharing (30, 39, 43, 52–55) were found to describe experimental observations better (43, 56, 57). The next improvement to the model was to explicitly consider that motors are bound to a three dimensional spherical cargo surface, that was typically considered rigid (58, 59). Only a couple of recent models have attempted to consider the lipid membrane on the cargo surface (41, 42).

Our model is a stochastic model that considers unequal load sharing with explicit implementation of motor diffusion on the cargo surface. In our model, we consider a spherical cargo of radius, $R = 250$ nm which is decorated with a given number of molecular motors (N) on the surface. N doesn't change during the cargo run, meaning there is no binding and unbinding of motors between the cargo surface and the solution. Each of these N motors is initially assigned a random, uniformly distributed anchor position on the cargo surface. Molecular motors on rigid cargo are fixed on the cargo surface. So a given initial configuration of motors on the rigid cargo surface persists throughout the cargo run whereas motors on lipid cargo diffuse on the surface.

In this study we considered that all N motors are kinesin motors which have a rest length of $L_{mot} = 57$ nm (46). We assume that an unbound kinesin motor binds to the microtubule with constant rate, $\pi_0 = 5\ \mathrm{s}^{-1}$ (39), if some part of the microtubule is within L_{mot} distance from the anchor position of that unbound motor. In other words, unbound motors bind with a specific rate to the microtubule if they can access the microtubule.

A microtubule bound motor is characterized by two position vectors, anchor point ($\vec{A}$) on the cargo surface and head ($\vec{H}$) on the microtubule. A microtubule bound motor is assumed to exert a spring-like force when the length of motor exceeds the motor's rest length (L_{mot}) with a force constant, $k_{mot} = 0.32$ pN/nm (60, 61). The force exerted by a motor on the cargo is then given by,

$$\vec{F} = -k_{mot}(\vec{A} - \vec{H}) \quad |\vec{A} - \vec{H}| > L_{mot} \qquad [2]$$

$$= 0 \qquad |\vec{A} - \vec{H}| \leq L_{mot} \qquad [3]$$

The translation velocity of the center of mass of cargo is given by the (overdamped) Langevin equation

$$\frac{d\vec{X}}{dt} = \frac{1}{\gamma_c}\left[\sum_{j=1}^{N} \vec{F}_j + \vec{F}_{steric}\right] + \vec{\zeta} \qquad [4]$$

Here, $\vec{F}_j$ is the force exerted on cargo by the jth motor. $\vec{F}_{steric}$ is the spring-like steric force on the cargo from the microtubule, represented with a high force constant $10k_{mot}$. We note that if the vesicle is deformable the steric spring constant could be significantly smaller. This force is present only if the cargo-microtubule distance is less than the sum of the cargo and microtubule radii. $\vec{\zeta}$ is the random force on the cargo due to collisions with the intracellular medium. We assume a normally distributed noise with zero mean, $\langle\vec{\zeta}\rangle = 0$ and the fluctuation-dissipation relation, $\langle\zeta_\mu(t)\zeta_\nu(t')\rangle = 2\gamma_c k_B T \delta_{\mu\nu}\delta(t - t')$. γ_c is the friction co-efficient for the cargo given by $\gamma_c = 18\pi\eta_v R$, where η_v is the co-efficient of viscosity of cytoplasm experienced by cargo. We approximated η_v to be equal to the co-efficient of viscosity of water, $\eta_v = 10^{-3}$ Pa.s. We integrate Eq. 4 using the Euler-Maruyama scheme

$$\vec{X}(t + \Delta t) = \vec{X}(t) + \frac{\Delta t}{\gamma_c}\left[\sum_{j=1}^{N} \vec{F}_j + \vec{F}_{steric}\right] + \sqrt{2\gamma_c k_B T \Delta t}\vec{\xi} \qquad [5]$$

where $\vec{\xi} = (\xi_1, \xi_2, \xi_3)$ and ξ_1, ξ_2, ξ_3 are drawn from normal distribution with zero mean and unit variance.

At each time step we also update the anchor positions of each motor on the lipid cargo surface using a similar Brownian dynamics formalism given by

$$\vec{A}(t + \Delta t) = \vec{A}(t) + \Delta l_\theta \hat{\theta} + \Delta l_\phi \hat{\phi} \qquad [6]$$

where Δl_θ and Δl_ϕ are the small displacements along $\hat{\theta}$ and $\hat{\phi}$ directions in the plane tangential to cargo surface at $\vec{A}(t)$. Δl_θ and Δl_ϕ are given by

$$\begin{pmatrix}\Delta l_\theta \\ \Delta l_\phi\end{pmatrix} = \sqrt{2D\Delta t}\begin{pmatrix}\xi_a \\ \xi_b\end{pmatrix} + \frac{\Delta t}{\gamma_s}\begin{pmatrix}f_\theta \\ f_\phi\end{pmatrix} \qquad [7]$$

where ξ_a and ξ_b are random variables obtained from normal distribution with zero mean and unit variance. D is the diffusion constant for motor diffusion on cargo surface and γ_s is the friction coefficient given by $\gamma_s = k_B T/D$. (f_θ, f_ϕ) are the components of motor forces along $\hat{\theta}$ and $\hat{\phi}$ respectively which can be obtained from the motor force in Cartesian co-ordinates, $\vec{F} = (f_x, f_y, f_z)$ as follows

$$\begin{pmatrix}f_\theta \\ f_\phi\end{pmatrix} = \begin{pmatrix}\cos\theta\cos\phi & \cos\theta\sin\phi & -\sin\theta \\ -\sin\phi & \cos\phi & 0\end{pmatrix}\begin{pmatrix}f_x \\ f_y \\ f_z\end{pmatrix} \qquad [8]$$

At every time step, each bound kinesin motor hydrolyses an ATP molecule with certain probability and attempts to move forward on the microtubule. This stepping probability is a function of the motor force and also the ATP concentration. We have adopted the following relation for the stepping probability (44)

$$p_{step}([\mathrm{ATP}], \vec{F}) = 1 - e^{-v\Delta t/\delta} \qquad [9]$$

where δ is the step size, the distance moved by motor after hydrolyzing one ATP molecule ($\delta = 8$ nm (13, 62, 63)). v is the velocity of

kinesin motor which is a function of the ATP concentration and motor force and is taken to be

$$v(_{[\mathrm{ATP}]},\vec{F}) = v_0(_{[\mathrm{ATP}]})\tilde{v}(\vec{F}) \qquad [10]$$

where $v_0(_{[\mathrm{ATP}]})$ is the velocity of motor under no-load condition at a given ATP concentration. The ATP dependence of v_0 is described by the Michaelis-Menten equation

$$v_0(_{[\mathrm{ATP}]}) = \frac{v_{max}[ATP]}{K_m + [ATP]} \qquad [11]$$

We considered the no-load velocity at saturated ATP concentration to be $v_{max} = 800$ nm/s (44, 45) and $K_m = 44\,\mu$M (64).

$\tilde{v}(\vec{F})$ gives the force dependence of the velocity. In the hindering direction, we assume (43, 44)

$$\begin{aligned} \tilde{v}_{hind}(\vec{F}) &= \left[1 - \left(\frac{F}{F_s}\right)^w\right] & F < F_s \\ &= 0 & F \geq F_s \end{aligned} \qquad [12]$$

F is the magnitude of motor force, $F = |\vec{F}|$. F_s is the stall force, the value of force beyond which kinesin motor stops walking. We considered $F_s = 7$ pN (45, 65, 66) and $w = 2$ (56). In the assistive direction, velocity is assumed to be independent of force magnitude, $\tilde{v}_{asst}(\vec{F}) = 1$ (44, 45).

Experimentally it is found that a kinesin motor is more likely to detach from the microtubule when one head is detached from the microtubule while trying to take a step than when both the heads are bound to the microtubule (64, 67, 68). In our model we assume that a motor can detach only when it tries to take a step. At every time step we first check whether a bound motor tries to make a step with probability $p_{step}(_{[\mathrm{ATP}]},\vec{F})$ using Eq. 9. If it tries to take a step, we check whether it detaches from the microtubule before completing the step using a microscopic off-rate whose value is calibrated based on the experimentally observed off-rate as a function of force, F, at saturating ATP concentrations.

$$\epsilon_{micro}(\vec{F}) = \frac{\epsilon_{obs}(\vec{F})}{p_{step}(_{[\mathrm{ATP}]=2\,\mathrm{mM}},\vec{F})} \qquad [13]$$

$p_{step}(_{[\mathrm{ATP}]=2\,\mathrm{mM}},\vec{F})$ is the probability to step forward in time step Δt at high ATP concentration of 2 mM.

For hindering forces, we used the following relationship between observed off-rate and magnitude of motor force F developed in (15) based on Kramer's theory (69) and used in several studies (23, 43, 44)

$$\epsilon_{obs}^{hind}(\vec{F}) = \epsilon_0 e^{F/F_d} \qquad [14]$$

ϵ_0 is the off-rate under no load condition. We used $\epsilon_0 = 0.79\,s^{-1}$ (44, 45). F_d is the detachment force. We approximated F_d to be equal to the stall force F_s. For assistive forces, the relationship between observed off-rate and magnitude of force is taken to be (44, 45)

$$\epsilon_{obs}^{asst}(\vec{F}) = \epsilon_0 + 1.56 \times 10^{12} F \qquad [15]$$

ACKNOWLEDGMENTS. We thank helpful discussions with David Quint and Jing Xu. This work was supported by the National Science Foundation (NSF-DMS-1616926) and NSF-CREST: Center for Cellular and Bio-molecular Machines at UC Merced (NSF-HRD-1547848). We also acknowledge partial support from the NSF Center for Engineering Mechanobiology grant CMMI-154857 and computing time on the Multi-Environment Computer for Exploration and Discovery (MERCED) cluster at UC Merced (NSF-ACI-1429783). NS acknowledges Graduate Student Opportunity Program Fellowship from the University of California Merced.

1. Howard J (2001) *Mechanics of motor proteins and the cytoskeleton.* (Sinauer Associates (OUP)).
2. O'Connor CM, Adams JU (2010) *Essentials of cell biology.* (NPG Education, Cambridge, MA).
3. Ross JL, Ali MY, Warshaw DM (2008) Cargo transport: molecular motors navigate a complex cytoskeleton. *Curr Opin Cell Biol* 20(1):41–107.
4. Sabharwal V, Koushika SP (2019) Crowd Control: Effects of Physical Crowding on Cargo Movement in Healthy and Diseased Neurons. *Front Cell Neurosci* 13:470.
5. Lakadamyali M (2014) Navigating the cell: how motors overcome roadblocks and traffic jams to efficiently transport cargo. *Phys Chem Chem Phys* 16:5907.
6. Grundke-Iqbal I, et al. (1986) Abnormal phosphorylation of the microtubule-associated protein tau (tau) in Alzheimer cytoskeletal pathology. *Proc. Natl. Acad. Sci. U.S.A.* 83(13):4913–4917.
7. Iqbal K, Liu F, Gong CX, Grundke-Iqbal I (2010) Tau in Alzheimer Disease and Related Tauopathies. *Curr. Alzheimer Res.* 7(8):656–664.
8. Chevalier-Larsen E, Holzbaur EL (2006) Axonal transport and neurodegenerative disease. *Biochim. Biophys. Acta Mol. Basis Dis.* 1762(11):1094 – 1108. Molecular Basis of Amyotrophic Lateral Sclerosis.
9. Millecamps S, Julien JP (2013) Axonal transport deficits and neurodegenerative diseases. *Nat. Rev. Neurosci.* 14(3):161–176.
10. Langford GM (1995) Actin- and microtubule-dependent organelle motors: interrelationships between the two motility systems. *Curr. Opin. Cell. Biol.* 7(1):82–88.
11. Svoboda K, Block SM (1994) Force and velocity measured for single kinesin molecules. *Cell* 77(5):773–784.
12. Visscher K, Schnitzer MJ, Block SM (1999) Single kinesin molecules studied with a molecular force clamp. *Nature* 400(6740):184–189.
13. Yildiz A, Tomishige M, Vale RD, Selvin PR (2004) Kinesin walks hand-over-hand. *Science* 303(5658):676–678.
14. Andreasson JOL, et al. (2015) Examining kinesin processivity within a general gating framework. *eLife* 4.
15. Schnitzer MJ, Visscher K, Block SM (2000) Force production by single kinesin motors. *Nat. Cell. Biol.* 2(10):718–723.
16. Sellers JR, Veigel C (2006) Walking with myosin v. *Curr. Opin. Cell Biol.* 18(1):68 – 73. Cell structure and dynamics.
17. Block SM (2007) Kinesin motor mechanics: Binding, stepping, tracking, gating, and limping. *Biophys. J.* 92(9):2986–2995.
18. Ally S, Larson AG, Barlan K, Rice SE, Gelfand VI (2009) Opposite-polarity motors activate one another to trigger cargo transport in live cells. *J. Cell Biol.* 187(7):1071–82.
19. Holzbaur EL, Goldman YE (2010) Coordination of molecular motors: from in vitro assays to intracellular dynamics. *Curr. Opin. Cell Biol.* 22(1):4–13.
20. Shubeita GT, et al. (2008) Consequences of Motor Copy Number on the Intracellular Transport of Kinesin-1-Driven Lipid Droplets. *Cell* 135(6):1098–1107.
21. Mallik R, Gross SP (2004) Molecular motors: strategies to get along. *Curr. Biol.* 14(22):R971–R982.
22. Klumpp S, Nieuwenhuizen TM, Lipowsky R (2005) Movements of molecular motors: ratchets, random walks and traffic phenomena. *Physica E* 29(1–2):380–389.
23. Klumpp S, Lipowsky R (2005) Cooperative cargo transport by several molecular motors. *Proc. Natl. Acad. Sci. U.S.A.* 102(48):17284–17289.
24. Beeg J, Klumpp S, Dimova R, S.Garcia R, Unger E (2008) Transport of beads by several kinesin motors. *Biophys. J.* 94(2):532–541.
25. Müller MJI, Klumpp S, Lipowsky R (2008) Tug-of-war as a cooperative mechanism for bidirectional cargo transport by molecular motors. *Proc. Natl. Acad. Sci. U.S.A.* 105(12):4609–4614.
26. Ando D, Mattson M, Xu J, Gopinathan A (2014) Cooperative protofilament switching emerges from inter-motor interference in multiple-motor transport. *Sci. Rep.* 4:7255.
27. Huang K, Vega C, Gopinathan A (2011) Conformational changes, diffusion and collective behavior in monomeric kinesin-based motility. *J. Phys. Condens. Matter* 23(37):374106.
28. Driver JW, et al. (2010) Coupling between motor proteins determines dynamic behaviors of motor protein assemblies. *Phys. Chem. Chem. Phys.* 12(35):10398.
29. Rogers AR, Driver JW, Constantinou PE, Jamison DK, Diehl MR (2009) Negative interference dominates collective transport of kinesin motors in the absence of load. *Phys. Chem. Chem. Phys.* 11(24):4800–4803.
30. Jamison DK, Driver JW, Rogers AR, Constantinou PE, Diehl MR (2010) Two kinesins transport cargo primarily via the action of one motor: Implications for intracellular transport. *Biophys. J.* 99(9):2967–2977.
31. Peker I, Granek R (2016) Multimotor Driven Cargos: From Single Motor under Load to the Role of Motor-Motor Coupling. *J. Phys. Chem. B* 120(26):6319–6326.
32. McLaughlin RT, Diehl MR, Kolomeisky AB (2016) Collective dynamics of processive cytoskeletal motors. *Soft Matter* 12(1):14–21.
33. Maday S, Twelvetrees AE, Moughamian AJ, Holzbaur EL (2014) Axonal transport: Cargo-specific mechanisms of motility and regulation. *Neuron* 84(2):292–309.
34. Barlan K, Rossow MJ, Gelfand VI (2013) The journey of the organelle: teamwork and regulation in intracellular transport. *Curr. Opin. Cell Biol.* 25(4):483–488. Cell organelles.
35. Efremov AK, et al. (2014) Delineating cooperative responses of processive motors in living cells. *Proc. Natl. Acad. Sci. U.S.A.* 111(3):E334–E343.
36. Grover R, et al. (2016) Transport efficiency of membrane-anchored kinesin-1 motors depends on motor density and diffusivity. *Proc. Natl. Acad. Sci. U.S.A.* 113(46):E7185–E7193.
37. Lopes J, et al. (2019) Membrane mediated motor kinetics in microtubule gliding assays. *Sci. Rep.* 9(1).
38. Jiang R, et al. (2019) Microtubule binding kinetics of membrane-bound kinesin-1 predicts high motor copy numbers on intracellular cargo. *Proc. Nat. Acad. Sci. U.S.A.* 116(52):26564–26570.
39. Leduc C, et al. (2004) Cooperative extraction of membrane nanotubes by molecular motors. *Proc. Natl. Acad. Sci. U.S.A.* 101(49):17096–17101.
40. Li Q, Tseng KF, King SJ, Qiu W, Xu J (2018) A fluid membrane enhances the velocity of cargo transport by small teams of kinesin-1. *J. Chem. Phys.* 148(12):123318.
41. Nelson SR, Trybus KM, Warshaw DM (2014) Motor coupling through lipid membranes enhances transport velocities for ensembles of myosin Va. *Proc. Natl. Acad. Sci. U.S.A.* 111(38):E3986–E3995.
42. Bovyn M, Janakaloti Narayanareddy BR, Gross S, Allard J (2021) Diffusion of kinesin motors on cargo can enhance binding and run lengths during intracellular transport. *Mol. Biol. Cell.* 32(9):984–994. PMID: 33439674.
43. Kunwar A, Mogilner A (2010) Robust transport by multiple motors with nonlinear force– velocity relations and stochastic load sharing. *Phys. Biol.* 7(1):16012.
44. Arpag G, Shastry S, Hancock WO, Tüzel E (2014) Transport by populations of fast and slow

kinesins uncovers novel family-dependent motor characteristics important for in vivo function. *Biophys. J.* 107(8):1896–1904.
45. Andreasson JOL (2013) Ph.D. thesis (Stanford University, Stanford,CA).
46. Li Q, King SJ, Gopinathan A, Xu J (2016) Quantitative Determination of the Probability of Multiple-Motor Transport in Bead-Based Assays. *Biophys. J.* 110(12):2720–2728.
47. Joyner RP, et al. (2016) A glucose-starvation response regulates the diffusion of macromolecules. *eLife* 5:e09376.
48. Chen X, Williams JA (2004) Exocytosis in *Encyclopedia of Gastroenterology*.
49. Klaus CJS, Raghunathan K, DiBenedetto E, Kenworthy AK (2016) Analysis of diffusion in curved surfaces and its application to tubular membranes. *Mol. Biol. Cell* 27(24):3937–3946. PMID: 27733625.
50. Grover R, et al. (2016) Transport efficiency of membrane-anchored kinesin-1 motors depends on motor density and diffusivity. *Proc. Natl. Acad. Sci. U.S.A.* 113(46):E7185–E7193.
51. Müller MJ, Klumpp S, Lipowsky R (2010) Bidirectional transport by molecular motors: Enhanced processivity and response to external forces. *Biophys. J.* 98(11):2610–2618.
52. Kunwar A, Vershinin M, Xu J, Gross SP (2008) Stepping, Strain Gating, and an Unexpected Force-Velocity Curve for Multiple-Motor-Based Transport. *Curr. Biol.* 18(16):1173–1183.
53. Bouzat S, Falo F (2010) The influence of direct motor-motor interaction in models for cargo transport by a single team of motors. *Phys. Biol.* 7(4).
54. Zhang Y (2011) Cargo transport by several motors. *Phys. Rev. E* 83(1):011909.
55. Wilson JO, Quint DA, Gopinathan A, Xu J (2019) Cargo diffusion shortens single-kinesin runs at low viscous drag. *Sci. Rep.* 9(1):1–12.
56. Kunwar A, et al. (2011) Mechanical stochastic tug-of-war models cannot explain bidirectional lipid-droplet transport. *Proc. Natl. Acad. Sci. U.S.A.* 108(47):18960–18965.
57. Bouzat S, Falo F (2011) Tug of war of molecular motors: The effects of uneven load sharing. *Phys. Biol.* 8(6).
58. Bergman JP, et al. (2018) Cargo navigation across 3d microtubule intersections. *Proc. Natl. Acad. Sci. U.S.A.* 115(3):537–542.
59. Erickson RP, Jia Z, Gross SP, Yu CC (2011) How molecular motors are arranged on a cargo is important for vesicular transport. *PLoS Comput. Biol.* 7(5):e1002032.
60. Coppin CM, Pierce DW, Hsu L, Vale RD (1997) The load dependence of kinesin's mechanical cycle. *Proc. Natl. Acad. Sci. U.S.A.* 94(16):8539–8544.
61. Coppin CM, Finer JT, Spudich JA, Vale RD (1996) Detection of sub-8-nm movements of kinesin by high-resolution optical-trap microscopy. *Proc. Natl. Acad. Sci. U.S.A.* 93(5):1913–1917.
62. Block SM, Schnitzer MJ (1997) Kinesin hydrolyses one ATP per 8-nm step. *Nature* 388(6640):386–390.
63. Coy DL, Wagenbach M, Howard J (1999) Kinesin takes one 8-nm step for each ATP that it hydrolyzes. *J. Biol. Chem.* 274(6):3667–3671.
64. Xu J, Shu Z, King SJ, Gross SP (2012) Tuning Multiple Motor Travel via Single Motor Velocity. *Traffic* 13(9):1198–1205.
65. Carter NJ, Cross RA (2005) Mechanics of the kinesin step. *Nature* 435(7040):308–312.
66. Block SM, Asbury CL, Shaevitz JW, Lang MJ (2003) Probing the kinesin reaction cycle with a 2D optical force clamp. *Proc. Natl. Acad. Sci. U.S.A.* 100(5):2351–2356.
67. Yajima J, Alonso MC, Cross RA, Toyoshima YY (2002) Direct Long-Term Observation of Kinesin Processivity at Low Load. *Curr. Biol.* 12(4):301–306.
68. Seitz A, Surrey T (2006) Processive movement of single kinesins on crowded microtubules visualized using quantum dots. *EMBO J.* 25(2):267–277.
69. Kramers HA (1940) Brownian motion in a field of force and the diffusion model of chemical reactions. *Physica* 7(4):284–304.